Journal of Virus Eradication 12 (2026) 100624

Contents lists available at ScienceDirect

Journal of Virus Eradication

journal homepage: www.sciencedirect.com/journal/journal-of-virus-eradication

Original research

Single-cell transcriptomic profiling of the splenic and peripheral immune landscape in rhesus macaques during CHIKV infection

Yun Yang [a,d], Qing Huang [a,d], Hao Yang [a,d], Yanan Zhou [a], Junbin Wang [a], Cong Tang [a], Wenhai Yu [a], Haixuan Wang [a], Daoju Wu [a], Hongyu Chen [a], Bai Li [a], Wenqi Quan [a], Jiandong Shi [a,b,c,*], Qiangming Sun [a,b,c,**], Shuaiyao Lu [a,b,c,***]

[a] State Key Laboratory of Respiratory Health and Multimorbidity. Institute of Medical Biology, Chinese Academy of Medical Sciences & Peking Union Medical College (IMBCAMS&PUMC), 935 Jiaoling Road, Kunming, Yunnan 650118, China
[b] Yunnan Key Laboratory of Cross-Border Infectious Disease Control and Prevention and Novel Drug Development, Kunming, China
[c] Key Laboratory of Pathogen Infection Prevention and Control (Peking Union Medical College), Ministry of Education, Beijing, China

ARTICLE INFO

Keywords:
Chikungunya virus
Single-cell RNA sequencing
Neutrophil extracellular traps
Th1/Th17 differentiation
Acute phase

ABSTRACT

Chikungunya virus (CHIKV) is a re-emerging arbovirus causing acute febrile illness and chronic debilitating arthritis, thereby imposing significant global public health and economic burdens. While robust immune responses involving inflammatory cytokines and immune cell infiltration characterize acute infection, the cellular mechanisms underlying pathogenesis and chronicity remain incompletely defined. In this study, we employed single-cell RNA sequencing (scRNA-seq) to comprehensively profile splenic and peripheral blood mononuclear cells (PBMCs) immune responses in rhesus macaques at day 7 post CHIKV infection, an acute phase. Splenic neutrophils marked recruitment, upregulation of *S100A8/S100A9*, downregulation of interferon-stimulated genes (ISGs), and functional activation marked by degranulation, enhanced anti-apoptotic pathways, and neutrophil extracellular traps (NETs) formation, as visualized by multiplex immunofluorescence. Pseudotime trajectories delineated progressive states transitioning from proliferation to effector functions. Splenic T and B cells showed increased abundance with innate-to-adaptive transition signature. Splenic $CD4^+$ and $CD8^+$ T cell subsets and B cell subsets exhibited enrichment for innate immune pathways and translational machinery. In PBMCs, $CD8^+$ T cell subsets and B cell subsets exhibited activation of adhesion, cytokine signaling, and protein homeostasis pathways in infection group. Notably, CHIKV infection induced skewing of T cells toward states enriched for Th1 and Th17 differentiation (marked by *NXPE3, LEF1, NFKBIZ* expression) in PBMCs. These results delineate the spatiotemporal immune landscape during CHIKV acute phase, in this non-human primate model, identifying neutrophil-mediated inflammation, lymphocyte transcriptional adaptation, and Th1/Th17 polarization as hallmarks of acute phase, offering a detailed cellular map that may inform future investigations into CHIKV pathogenesis and therapeutic strategies.

1. Introduction

Chikungunya virus (CHIKV) is an arthropod-borne virus (arbovirus).[1] Infection typically causes Chikungunya fever (CHIKF), a clinical syndrome characterized by an acute onset of symptoms including fever, rash, joint pain, and musculoskeletal issues.[2] While most patients recover completely, chronic musculoskeletal symptoms persist in up to 40% of cases, with manifestations that can endure for years[3–5]. Such

* Corresponding author. Institute of Medical Biology, Chinese Academy of Medical Sciences & Peking Union Medical College (IMBCAMS&PUMC), 935 Jiaoling Road, Kunming, Yunnan 650118, China.
** Corresponding author. Institute of Medical Biology, Chinese Academy of Medical Sciences & Peking Union Medical College (IMBCAMS&PUMC), 935 Jiaoling Road, Kunming, Yunnan 650118, China.
*** Corresponding author. Institute of Medical Biology, Chinese Academy of Medical Sciences & Peking Union Medical College (IMBCAMS&PUMC), 935 Jiaoling Road, Kunming, Yunnan 650118, China.
E-mail addresses: dongdong9286@163.com (J. Shi), qsun@imbcams.com.cn (Q. Sun), lushuaiyao-km@163.com (S. Lu).
[d] These authors contribute equally.

https://doi.org/10.1016/j.jve.2026.100624
Received 24 February 2026; Received in revised form 23 March 2026; Accepted 24 March 2026
Available online 26 March 2026

chronic symptoms significantly reduce quality of life and impose a substantial economic burden. Owing to its capacity for rapid global spread, CHIKF represents a major threat to public health.[6] Since its first reported outbreak in Tanzania in 1952, CHIKV had been detected in more than 100 countries and territories by 2024, with over 4 million cases reported worldwide.[7,8]

Emerging evidence indicates that CHIKV-susceptible animals and humans mount a robust antiviral immune response during infection. During the acute phase, serum concentrations of inflammatory cytokines are significantly elevated, including type I & II Interferons (IFNγ, IFNα and IFN-β), interleukins (IL-1β, IL-2, IL-2R, IL-6, IL-7, IL-12, IL-15, IL-17 and IL-18) and chemokines (CXCL9 and CXCL10).[8,9] IFN signaling plays a key role in both viral replication and disease pathogenesis during acute infection.[9,10] As the infection progresses, a distinct panel of mediators becomes upregulated, including IL-6, MCP-1 (CCL2), IL-8 (CXCL8), MIP-1α (CCL3), and MIP-1β (CCL4).[11] Furthermore, CHIKV infection induces the infiltration of immune cells into synovial tissues, including monocytes, macrophages, neutrophils, and NK cells. This cellular influx, coupled with increased secretion of pro-inflammatory mediators, drives local tissue inflammation.[12,13]

Neutrophils are critical mediators of host defense. During viral infections, neutrophils are recruited to sites of inflammation by chemoattractant molecules produced by activated endothelial cells, resident immune cells, and injured epithelial cells[14–16]. Following engagement of pro-inflammatory signals with their surface receptors, neutrophils activate intracellular signaling cascades. Activated neutrophils exert their effector functions via several key mechanisms: degranulation (granules release), phagocytosis, internalization and degradation of pathogens, and the formation of neutrophil extracellular traps (NETs).[14] NETs are net-like DNA structures decorated with histones and antimicrobial proteins released by activated neutrophils. These structures function to entrap and eliminate a broad spectrum of pathogens.[17] Notably, murine studies reveal that NETosis (the process of NET formation) exerts antiviral effects during acute CHIKV infection by controlling systemic viral loads.[15]

Chikungunya virus (CHIKV)-associated arthritis and rheumatoid arthritis (RA) share similarities at the transcriptomic level as well as in cytokine and chemokine profiles.[18,19] Th1 and Th17 cells, two critical subsets of $CD4^+$ effector T cells, are implicated in the pathogenesis of RA ([20,21]). Th1 cells, which primarily secrete cytokines including IFN-γ and IL-2, are major contributors to autoimmune disorders.[22] Th17 cells, characterized by IL-17 secretion, drive autoimmunity, promote inflammatory conditions, and recruit neutrophils to infection sites.[18] Notably, research demonstrates that IL-17 plays a functional role not only during the acute phase of CHIKV infection in mice but also in the post-acute disease resolution phase.[23]

However, the cellular mechanisms underlying the immune response to CHIKV infection remain incompletely characterized. Single-cell RNA sequencing (scRNA-seq) technology has been extensively applied in virology research and offers substantial potential for yielding novel insights.[24,25] In this study, we performed scRNA-seq to comprehensively profile the immune landscape of splenic tissue and peripheral blood mononuclear cells (PBMCs) in rhesus macaques (*Macaca mulatta*) on day 7 post-CHIKV infection, with uninfected samples as controls. By evaluating immune signatures and compositional changes within the spleen and PBMCs, we characterize the immunological features marking the acute CHIKV infection. These findings provide critical insights that may guide therapeutic development against CHIKF.

2. Results

2.1. The scRNA-seq profiling of spleen and PBMCs with CHIKV infected and controls

Six adult rhesus monkeys of similar age were randomly divided into an infection group (n = 3) and a control group (n = 3). The infection group received an intramuscular injection of CHIKV (Accession: MH670649.1, 2×10^7 PFU) in the leg, while the control group received an equal volume of PBS via the same intramuscular route as a sham inoculation. During the experimental period, no typical clinical symptoms of CHIKV infection (such as rash, fever, and joint pain2) were observed in the infected group (Supporting Information 2). Spleen tissue and PBMCs were collected from both groups on day 7 post-infection for scRNA-seq (Fig. 1A). At this timepoint, viral loads were undetectable in peripheral blood but remained significantly elevated in the spleen (Supporting Information 1: Fig. S1A), consistent with previously reported animal models.[26,27] However, no viral RNA was detected in sequenced cells (Fig. S1B). We considered that this discrepancy might be due to the sensitivity limits of scRNA-seq for low-abundance viral transcripts or that, at day 7 post-infection, the number of cells actively transcribing viral RNA was below the detection threshold. After quality control, we analyzed 73,698 spleen cells (control: 43,873; infected: 29,825) and 60,409 PBMCs (control: 19,037; infected: 41,372). Dimensionality reduction and clustering using UMAP identified distinct cell types in spleen tissue and PBMCs (Fig. 1B and C, Supporting Information 1: Fig. S1C and D). Due to differences in cell markers between non-human primates and humans, we defined the cell populations primarily based on scRNA-seq studies of non-human primates[28,29] with additional reference to human cell markers documented in the CellMarker2.0 database.[30] In the spleen, major clusters included: $CD4^+$ T cell (expressing *CD3E*, *CCR7* and *ITM2A*), $CD8^+$ T cell (*CD3E*, *CCL5*), pre-B cell (*MKI67*, *CENPF*, *BANK1*), mature B cell (*MAB1*, *BANK1*), plasma B cell (ENSMMUG00000044861, ENSMMUG00000015202, *MAB1*), macrophage (*CFD*, *APOE*), neutrophil (*CFD*, S100A9), monocyte (*CFD*, *VCAM1*) and dividing NK cell (*NKG7*, *CENPF*, *MKI67*) (Fig. 1D & Supporting Information 1: Fig. S1E). In PBMCs, major clusters included: monocytes (*CFD*, *CST3*, *CD14*), erythrocyte (*HBA*, *HBE1*), endothelial cell (*CLDN5*, *CST3*), plasma B cell (*ENSMMUG00000044861*), T cell (*CD3E*, *CD3D*) and B cell 1and B cell 2 (*MS4A1*, *CD79A*) (Fig. 1E & Supporting Information 1: Fig. S1F). The two B cell subsets (B cell 1 and B cell 2) showed no differential expression in the B cell key marker. Their distinction is thus likely driven by differences in the expression of other genes. Therefore, these two clusters were combined for subsequent analysis.

Compared with control animals, CHIKV-infected rhesus monkey showed decreased proportions of splenic macrophages and mature B cells, but increased proportions of splenic neutrophils and $CD4^+$ T cells (Fig. 1F). In PBMCs, monocyte and T-cell frequencies increased following infection (Fig. 1G). Although most compositional shifts did not reach statistical significance, neutrophil enrichment in the spleen was statistically significant (Fig. 1H).

2.2. Neutrophils migrate to the spleen following CHIKV infection

H&E staining detected marked histological injury in the spleen, which was primarily characterized by bleeding and lymphocyte infiltration (Supporting Information 1: Fig. S2). Compared with controls, splenic neutrophils from CHIKV-infected rhesus monkey exhibited downregulation of interferon-stimulated genes (ISGs), including genes from the *IFIT* family (IFIT1, IFIT2, IFIT3), *MX* family genes (e.g., *MX1*, *MX2*), and *ISG15*. Conversely, upregulation was observed for genes encoding S100A8 and S100A9 (Fig. 2A). Functional enrichment analysis of the upregulated genes revealed significant enrichment for terms associated with neutrophil migration and infiltration. Key genes driving this enrichment included *SELL, DUSP1,* S100A8*, CSF3R, SPI1,* S100A9, and *LGALS3* (Fig. 2B). KEGG pathway analysis indicated significant enrichment for activated pathways, including FcγR-mediated phagocytosis, Ferroptosis, and Lysosome. Major contributing genes included *LIMK2, FCGR2B, FCGR2A, SAT1, ACSL1,* LOC719235*, SLC11A1,* and *LITAF* (Fig. 2C). Further subclustering identified 8 distinct neutrophil clusters. While no statistically significant infection-specific clusters emerged, the analysis revealed that the vast majority of splenic

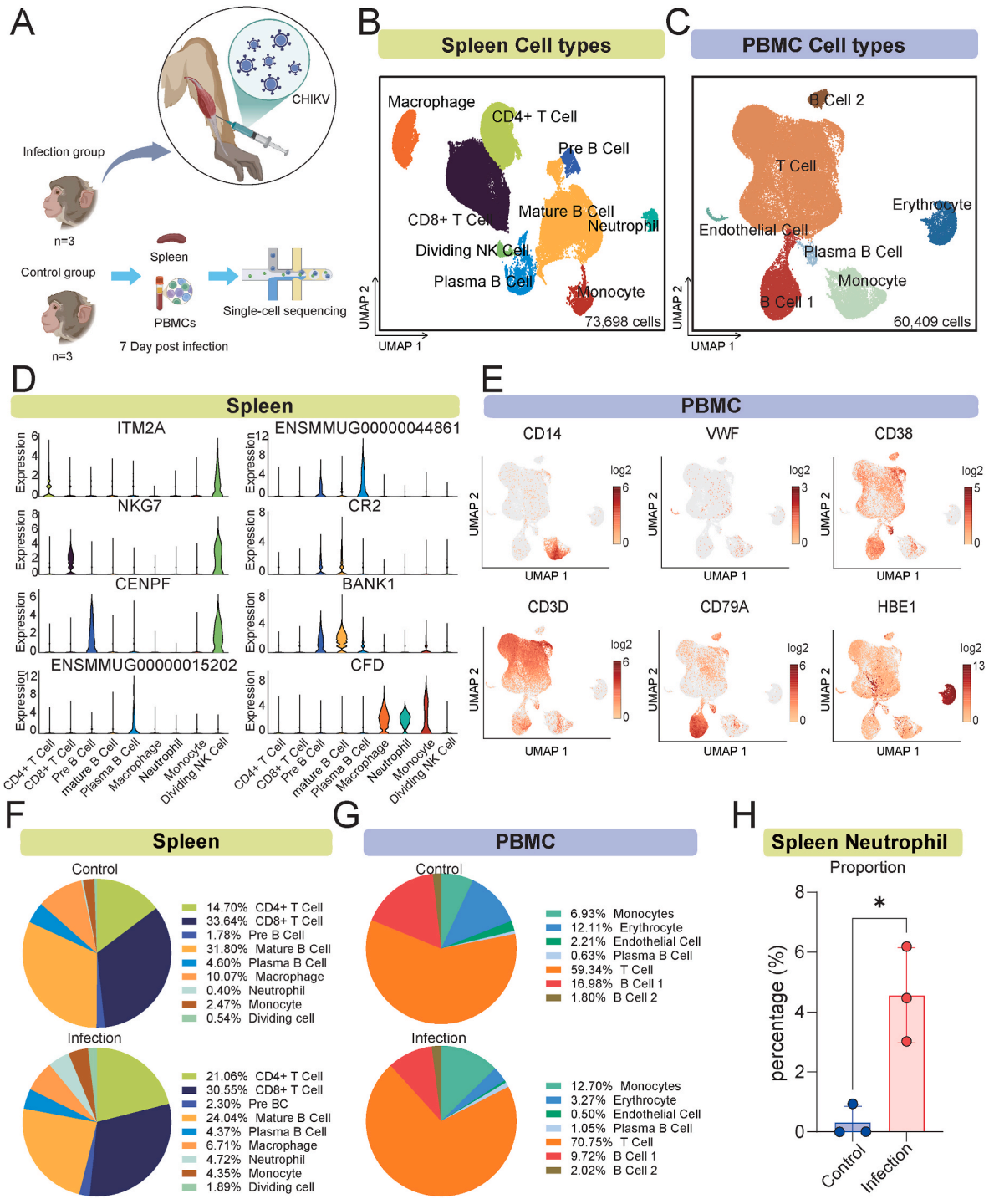

Fig. 1. The scRNA-seq reveals heterogeneity of spleen and PBMCs from CHIKV infected monkeys

A. Schematic depicting the study design, created with BioRender.com. Spleens and PBMCs of rhesus monkeys (n = 3) on day 7 post CHIKV infection were studied for scRNA-seq, and controls (n = 3) were injected with the same volume of PBS.

B. UMAP visualization of spleen (73,698 cells) cell types identified from gene expression data. Cells are colored by cell type identity and each dot represents a single cell.

C. UMAP visualization of PBMCs (60,409 cells) cell types identified from gene expression data. Cells are colored by cell type identity and each dot represents a single cell.

D. The violin plots of the expression of mark genes for spleen cell types.

E. Heatmap of the expression of marker genes for PBMCs cell types in the form of UMAP.

F. Pie charts of spleen cell type proportions (%) colored from UMAP.

G. Pie charts of PBMCs cell type proportions (%) colored from UMAP.

H. Bar chart comparing neutrophil proportions (%) between CHIKV infected (n = 3) and control groups (n = 3). Individual points represent biological replicates. Statistical significance determined by unpaired Mann-Whitney test. Statistical significance ($p \leq 0.05$) is indicated by "*". Error bars indicate SD.

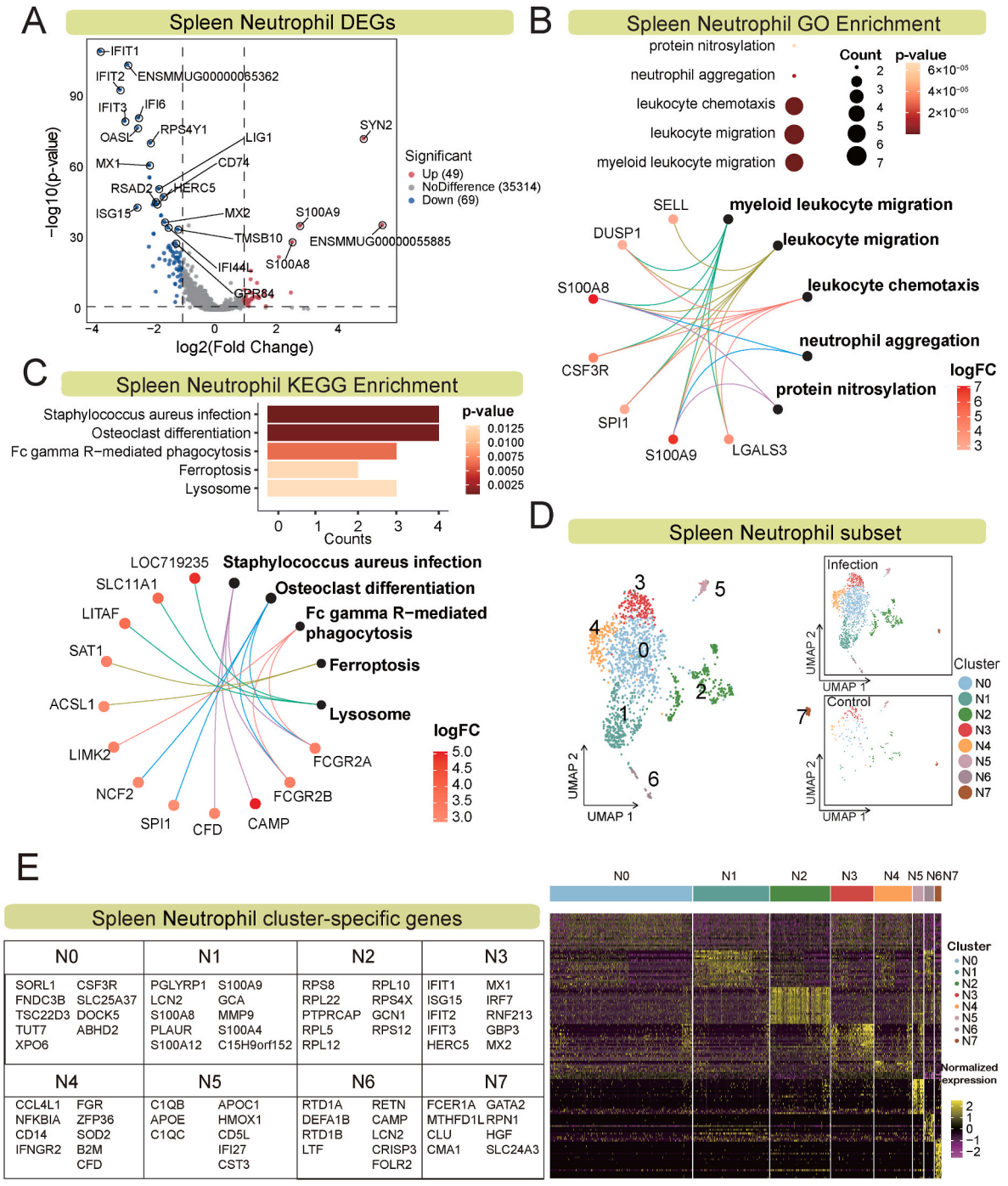

N0		N1		N2		N3	
SORL1	CSF3R	PGLYRP1	S100A9	RPS8	RPL10	IFIT1	MX1
FNDC3B	SLC25A37	LCN2	GCA	RPL22	RPS4X	ISG15	IRF7
TSC22D3	DOCK5	S100A8	MMP9	PTPRCAP	GCN1	IFIT2	RNF213
TUT7	ABHD2	PLAUR	S100A4	RPL5	RPS12	IFIT3	GBP3
XPO6		S100A12	C15H9orf152	RPL12		HERC5	MX2
N4		**N5**		**N6**		**N7**	
CCL4L1	FGR	C1QB	APOC1	RTD1A	RETN	FCER1A	GATA2
NFKBIA	ZFP36	APOE	HMOX1	DEFA1B	CAMP	MTHFD1L	RPN1
CD14	SOD2	C1QC	CD5L	RTD1B	LCN2	CLU	HGF
IFNGR2	B2M		IFI27	LTF	CRISP3	CMA1	SLC24A3
	CFD		CST3		FOLR2		

Fig. 2. Neutrophilic characteristics of the spleen after CHIKV infection

A. Volcano plot comparing neutrophils transcriptional profiles between infected and control groups. Each dot represents a gene, gray points: non-significant genes ($|\log_2$ Fold Change$| < 1.0$), blue points: significantly downregulated genes ($\log_2$ Fold Change ≤ -1.0, p-value ≤ 0.05), red points: significantly upregulated genes ($\log_2$ Fold Change ≥ 1.0, p-value ≤ 0.05).

B. Bubble plot of top 5 enriched GO biological processes for significantly upregulated genes (top panel), bubble size indicates gene count per term, color scale represents p-value. Term-gene network for enriched GO categories (bottom panel), black nodes represent GO terms, other nodes denote genes colored by $\log_{10}$FC.

C. Bar chart of top 5 enriched KEGG for significantly upregulated genes (top panel), bar length indicates gene count per term, color scale represents p-value. Term-gene network for enriched KEGG categories (bottom panel), black nodes represent KEGG terms, other nodes denote genes colored by $\log_{10}$FC.

D. UMAP visualization of neutrophils subclusters in spleen. Each dot represents a cell, colored by subclusters.

E. The heatmap displays the cluster-specific genes in each subcluster of Neutrophil cells in spleen. Each column represents a cell, and expression values are scaled by normalized expression.

neutrophils were recruited post-infection (Fig. 2D). The cluster-specific genes are shown in Fig. 2E.

2.3. CHIKV infection triggers neutrophils proliferation, anti-apoptotic effects, degranulation and NET formation in the spleen

To delineate developmental trajectories, we performed pseudotime

ordering on neutrophil cells using Monocle 2. Pseudotime trajectory analysis of splenic neutrophils revealed 7 distinct cellular states (Fig. 3A). Neutrophil subsets N0, N1, N3, and N4 were predominantly enriched in later stages of this pseudotime trajectory (Fig. 3B). Analysis of gene expression patterns across the trajectory identified six co-expression modules (Module1-6). Transcriptional analysis of the expanded neutrophil population revealed distinct states of activation. Modules 2, 4, 5, and 6 demonstrated high transcriptional activity, and characterized by robust expression of ribosomal genes, *RPL* and *RPS* families. Concurrently, cells in Modules 1 and 3 exhibited a shift toward a pro-inflammatory activated state (Supporting Information 1: Fig. S3A). Module1 was characterized by genes including *LTF*, *LCN2*, *CAMP*, and *GAPDH*. Module3 was characterized by genes including *MMP9*, S100A9, S100A4, S100A8, S100A6, *S100A12*, and *S100P* (Fig. 3C). Then we analyze the function of the neutrophil based on previously reported gene sets.[31,32] The transcriptional regulators associated with neutrophil precursors (preNeu; *IRF7*, *IRF9*, and *JUNB*) were expressed across subsets, with notably high expression levels (Fig. 3D). Neutrophils expanded post-infection exhibited an enhanced anti-apoptotic phenotype. Genes encoding *S100A8/S100A9* were significantly upregulated in subsets N0-N5 (Fig. 3E). Concurrently, expression of genes involved in granule production was induced, including *SLC11A1, ITGAM, CTSC, HEXA, CYBB, LCN2, ADAM8,* and *CFP* (Fig. 3F). To validate the observed neutrophil-specific gene expression patterns and functional state, we performed multiplex immunofluorescence for myeloperoxidase (MPO), citrullinated histone H3 (H3Cit), and CHIKV antigen. Results confirmed neutrophil infiltration within the spleen and the formation of neutrophil extracellular traps (NETs), characterized by co-localization of MPO, H3Cit, and CHIKV antigen (Fig. 3G & Supporting Information 1: Fig. S3B). This demonstrates that CHIKV infection triggers NET formation in splenic neutrophils.

2.4. Splenic T cells and B cells exhibit innate immune responses following CHIKV infection

Although T cells and B cells are central to adaptive antiviral immunity, UMAP visualization showed minimal overall compositional differences in splenic and PBMC T and B cell populations between CHIKV-infected and control groups. To uncover more subtle changes, we performed comparative transcriptomic analysis on T and B cell clusters in spleen (Fig. 4A). Subclustering identified 8 distinct T cell subsets (Spl_T0- Spl_T7) (Figs. 4B) and 11 distinct B cell subsets (Spl_B0- Spl_B10) (Fig. 4C). Analysis revealed increased proportions of T cell subsets T1, T2, T3, and T5, and B cell subsets Spl_B2, Spl_B4, Spl_B5, and Spl_B6 in infection group compared to controls, although these changes were not statistically significant (Fig. 4D). Phenotypic characterization identified T1 as a $CD4^+$ subset, while T2, T3, and T5 were $CD8^+$ cytotoxic subsets (Fig. 4E). To define the molecular features of each subset, we analyzed cluster-specific genes. Heatmaps displaying the cluster-specific genes per cluster revealed biologically relevant signatures (Fig. 4F & Supporting Information 1: Fig. S4A). Strikingly, all T cell subsets exhibited significant enrichment for innate immune-related Gene Ontology (GO) terms, including defense response to other organism, cellular response to interferon-gamma, response to other organism, and response to external biotic stimulus. Furthermore, subsets T3 and T7 specifically showed enrichment for GO terms related to cytoplasmic translational initiation and translational initiation (Fig. 4G). In B cell GO analysis, subset Spl_B2 was enriched for p38MAPK cascade. Subsets Spl_B4, Spl_B5, and Spl_B6 showed enrichment for GO terms associated with protein localization to endoplasmic reticulum, electron transport chain, and cellular respiration (Supporting Information 1: Fig. S4B). KEGG pathway analysis confirmed innate immune activation, subsets Spl_T1, Spl_T2, and Spl_T5 demonstrated activation of the natural killer cell mediated cytotoxicity pathway (Fig. 4H). Additionally, Subsets Spl_B2, Spl_B4, and Spl_B6 exhibited activation of the hematopoietic cell lineage pathway (Supporting Information 1: Fig. S4C).

2.5. Splenic T and B cell show an ongoing transition from innate to adaptive immunity

To delineate developmental trajectories, we performed pseudotime ordering on splenic T and B cells using Monocle 2. Analysis revealed 7 pseudotime states for T cells (Fig. 5A) and 3 states for B cells (Fig. 5B), as indicated by the heatmap in the upper-right corner, progression direction. In T cells, subsets that showed increased abundance post-infection were primarily localized to later pseudotime states. Specifically, Spl_T1 and Spl_T3 were largely found in State 2, while Spl_T2 and Spl_T5 were predominantly located in State 7 (Fig. 5C). In B cell, the increased subsets Spl_B5 and Spl_B6 were enriched within State 3 (Fig. 5C). Furthermore, quantification of cell proportions within pseudotime states showed no statistically significant differences in distribution between infected and control groups for either T or B cells.

Along the T cell pseudotime trajectory, dynamically expressed genes clustered into six co-expression modules. The GO enrichment revealed that Modules 1, 2 and 6 were enriched for functions associated with suppressed homeostatic immunity, including lymph node development and STAT-mediated cell surface receptor signaling. Conversely, Modules 3, 4 and 5 showed enrichment for functions reflecting enhanced effector immunity, including immune response, antigen processing and presentation, inflammatory response, and neutrophil chemotaxis (Fig. 5D). This transition shows T cell polarization into a pro-inflammatory state. Key driver genes associated with the immune, inflammatory, and chemotaxis functions in Module 5 included *TRBV24-1*, *FCER1G, CX3CR1, GZMA, KLF3, XCL1, HOPX,* ENSMMUG00000054501, *BHLHE40, TRGV10, TNFRSF1B*, ENSMMUG00000013779 (Supporting Information 1: Fig. S5A).

GO enrichment analysis revealed that genes in early B cells were distributed across modules 2, 4, 5, and 6, which contained relatively few genes and were associated with a state of lower metabolic and transcriptional activity. In contrast, later pseudotime stages were characterized by the expression of modules 1 and 3. These modules were linked to enhanced protein translation machinery (as evidenced by enrichments in nucleosome assembly and chromosome condensation) and the concurrent activation of both innate and adaptive immune systems, including immunoglobulin-mediated immunity, adaptive immune response, and innate immune response (Fig. 5E). Key genes associated with these functions included CENPF, *MKI67, MZB1, IGHV3-49*, and *IFI27* (Supporting Information 1: Fig. S5B).

2.6. T cell surface receptor activation and B cell translation are enhanced in PBMCs

We also performed a subclustering analysis of T and B cells within PBMCs (Fig. 6A). Subclustering identified 6 T cell subsets (PBMC_T0- PBMC_T5) (Figs. 6B) and 4 B cell subsets (PBMC_B0- PBMC_B3) (Fig. 6C). Quantitative analysis revealed increased proportions of the T cell subsets PBMC_T0, PBMC_T1, and PBMC_T4, as well as the B cell subsets PBMC_B2 and PBMC_B3, following CHIKV infection (Fig. 6D). Hematological parameters were also monitored in rhesus macaques by CBC at the time of PBMC isolation. No significant alterations were observed in total white blood cell counts, leukocyte subsets, or other indices on day 7 post-CHIKV infection (Supporting Information 1: Fig. S6A–B & Supporting Information 3).

Phenotypic characterization defined T0 as $CD4^+$ and $CD8^+$ double-positive cells and T1/T4 as $CD8^+$ populations (Fig. 6E). Heatmaps of cluster-specific marker genes revealed functionally relevant transcriptional signatures across subsets (Fig. 6F & S6C). Specifically, PBMC_T0 enrichment for *RCAN3*, *CR1 (CD35)*, *GPHN*, *CA6*, *CD28*, *ITGA6 (CD49f)*, *SELL (CD62L)*, *CCR7*, *IL6ST (CD130)*, and *LEF1*; PBMC_T1 enrichment for *GPR141, NKG7, TBX21* (T-bet)*, CST7, CLIC5, CX3CR1, IL7R (CD127)*, and *GZMB*; PBMC_T4 enrichment for the proliferation marker *MKI67* (suggestive of NKT-like cells); PBMC_B2 enrichment for *GZMM, IL7R (CD127)*, and *VCAN*; and PBMC_B3 enrichment for *JCHAIN,*

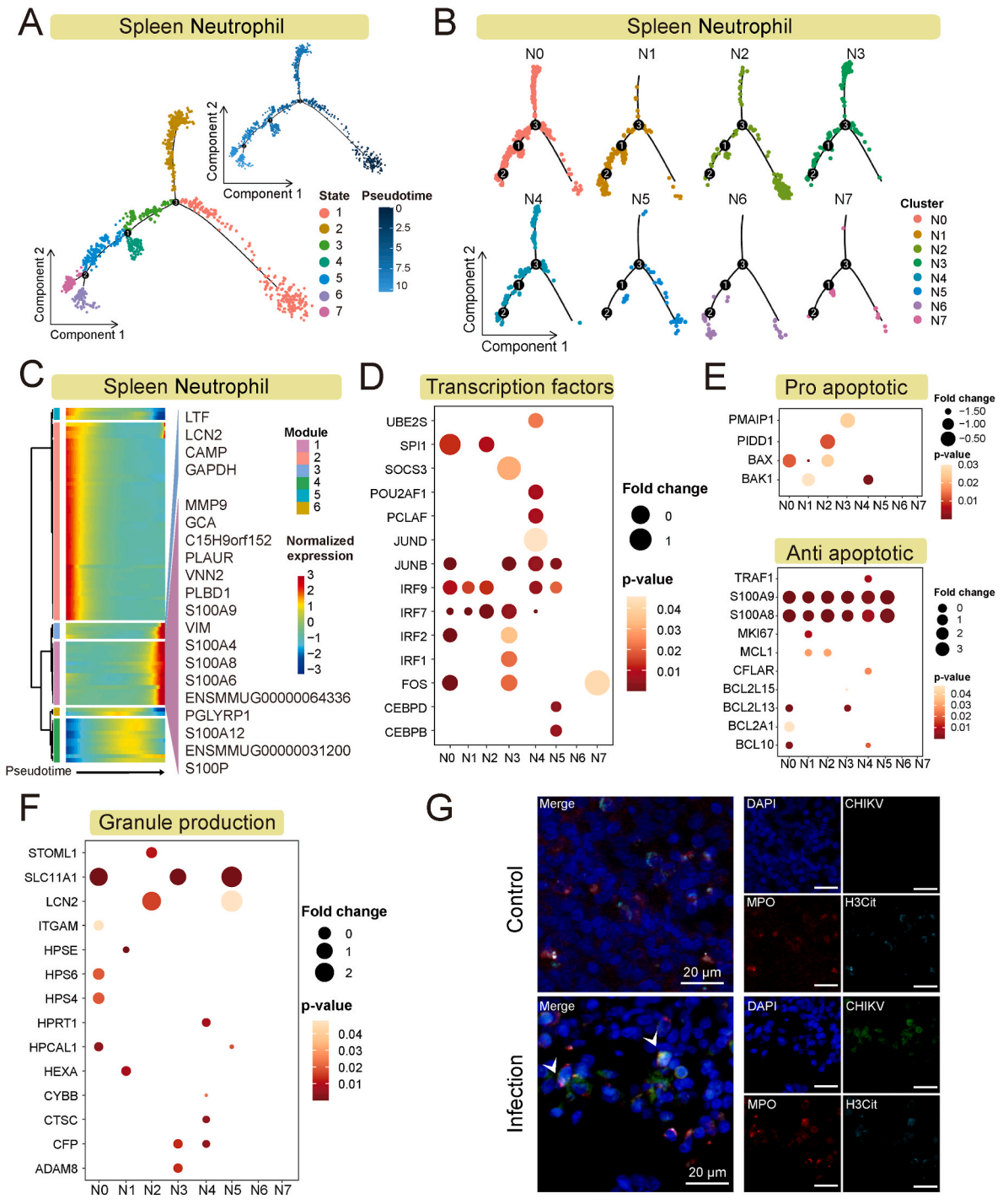

Fig. 3. Pseudotime trajectory and functional characterization of neutrophil heterogeneity

A. Pseudotime state visualization of neutrophils subclusters, colored by states. Each dot represents a single cell. The heat map of pseudotime progression is shown in the upper right corner.

B. Pseudotime state visualization of neutrophils cell subclusters, displayed separately for each cell cluster in Fig. 2E. The pseudotime progression is the same as in A.

C. Heatmap of the significantly differentially expressed genes during pseudotime progression of neutrophils.

D. Bubble plot of genes in transcription factors from neutrophil subclusters.

E. Bubble plot of genes in pro-apoptotic and anti-apoptotic from neutrophil subclusters.

F. Bubble plot of genes in granule production from neutrophil subclusters. In D, E and F, Bubble size indicates fold change, colored by p-value.

G. Immunofluorescence of NETs in spleen. DAPI (blue); MPO (red); CHIKV (green); histone H3 (cyan), the locations that were triple-positive for MPO, CHIKV, and histone H3 are indicated with white markers. Scale bar: 20 μm.

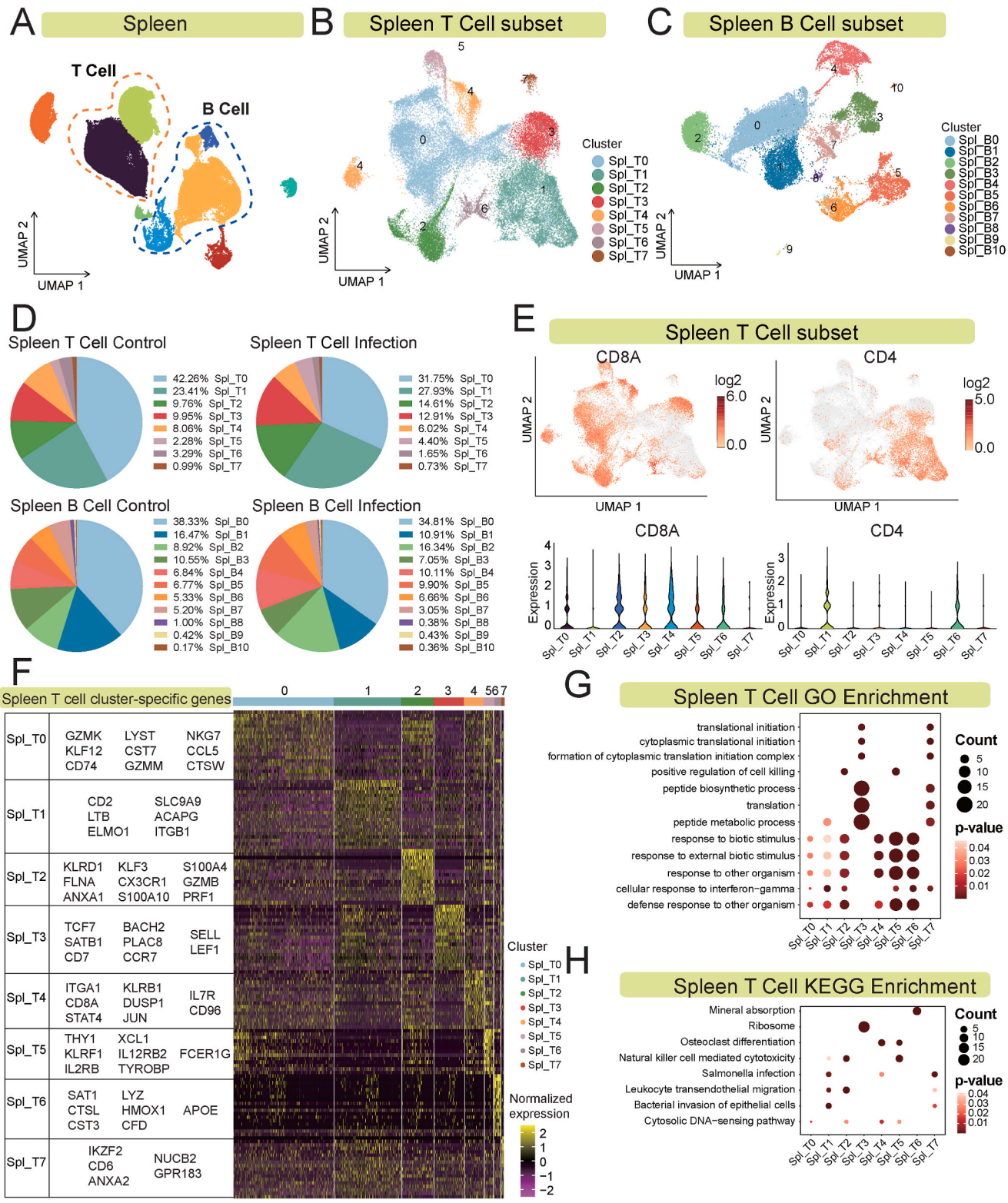

Fig. 4. Comprehensive analysis of T and B cell subpopulations in spleen

A. Schematic depicting the splenic T cells and B cells subcluster analysis.

B. UMAP visualization of T cell subclusters in spleen. Each dot represents a cell, colored by subclusters.

C. UMAP visualization of B cell subclusters in spleen. Each dot represents a cell, colored by subclusters.

D. Pie charts of T cell (top panel) and B (bottom panel) cell subclusters proportions (%) colored from B or C.

E. The heatmap (top panel) and violin plots (bottom panel) of the expression of CD8A and CD4 in T cell subclusters.

F. The heatmap displays the cluster-specific gene in each subcluster of T cells. Each column represents a cell, and expression values are scaled by normalized expression.

G. Bubble plots of GO biological processes enrichment comparative analysis of T cell subclusters. Bubble size indicates gene ratio; color scale represents p-value.

H. Bubble plots of KEGG enrichment comparative analysis of T cell subclusters. Bubble size indicates gene ratio; color scale represents p-value.

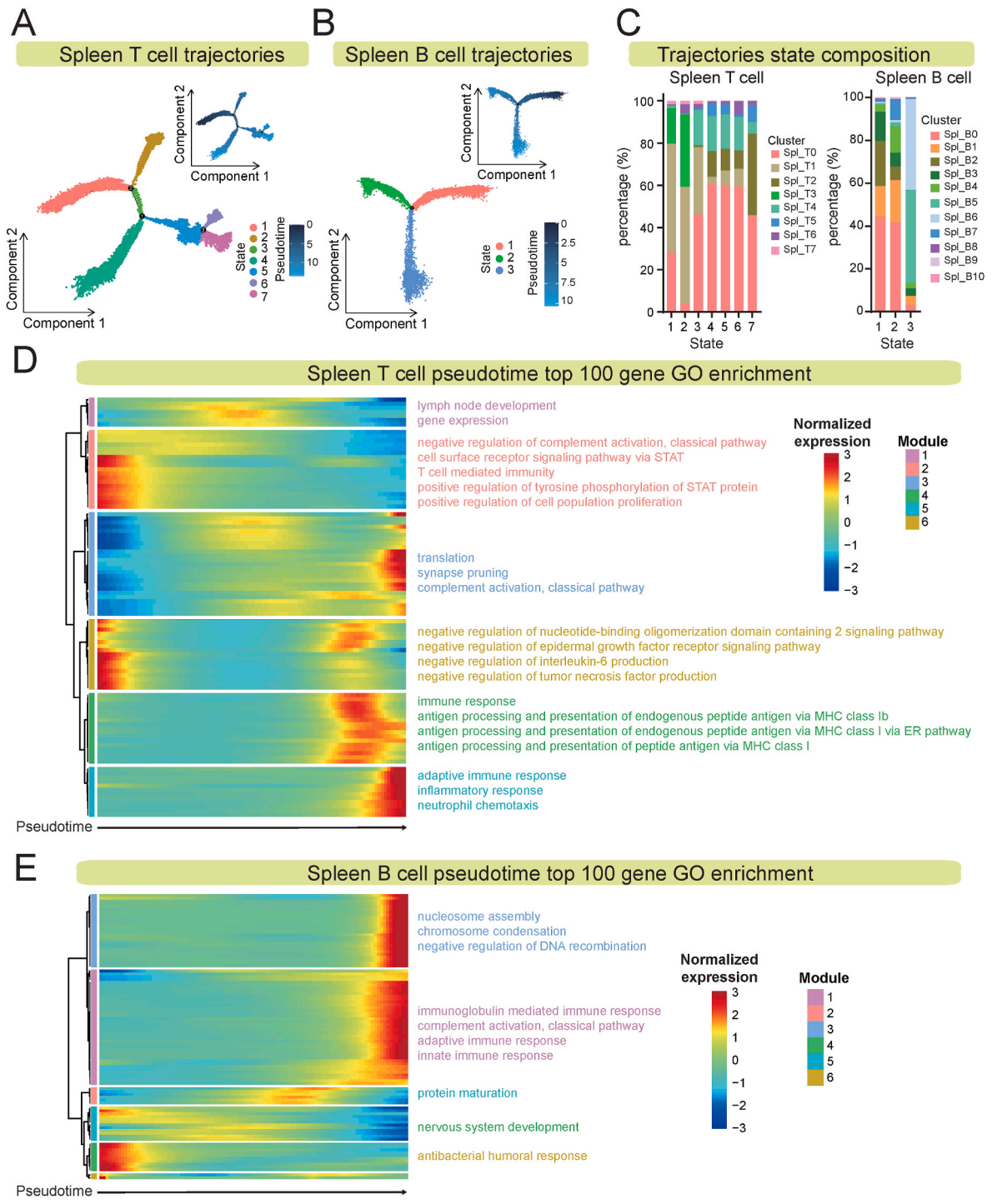

Fig. 5. Trajectory inference and functional characterization of T and B cell progression in spleen

A. Pseudotime state visualization of T cell subclusters in spleen, colored by each state. Each dot represents a single cell. The heat map of pseudotime progression is shown in the upper right corner.

B. Pseudotime state visualization of B cell subclusters in spleen, colored by each state. Each dot represents a single cell. The heat map of pseudotime progression is shown in the upper right corner.

C. Stacked bar chart showing proportional distribution of 8 T cell subclusters (Spl_T0- Spl_T7) across 7 pseudotime states (State 1-7) (left panel) and 11 B cell subclusters (Spl_B0- Spl_B10) across 3 pseudotime states (State 1-3) (right panel). Color-coding corresponds to subcluster identity as shown in legend.

D. Heatmap of the significantly differentially expressed top 100 genes during progression of T cell in spleen. The significant GO ($p \leq 0.05$) enriched functions of these genes are shown on the right.

E. Heatmap of the significantly differentially expressed top 100 genes during progression of B cell in spleen. The significant GO ($p \leq 0.05$) enriched functions of these genes are shown on the right.

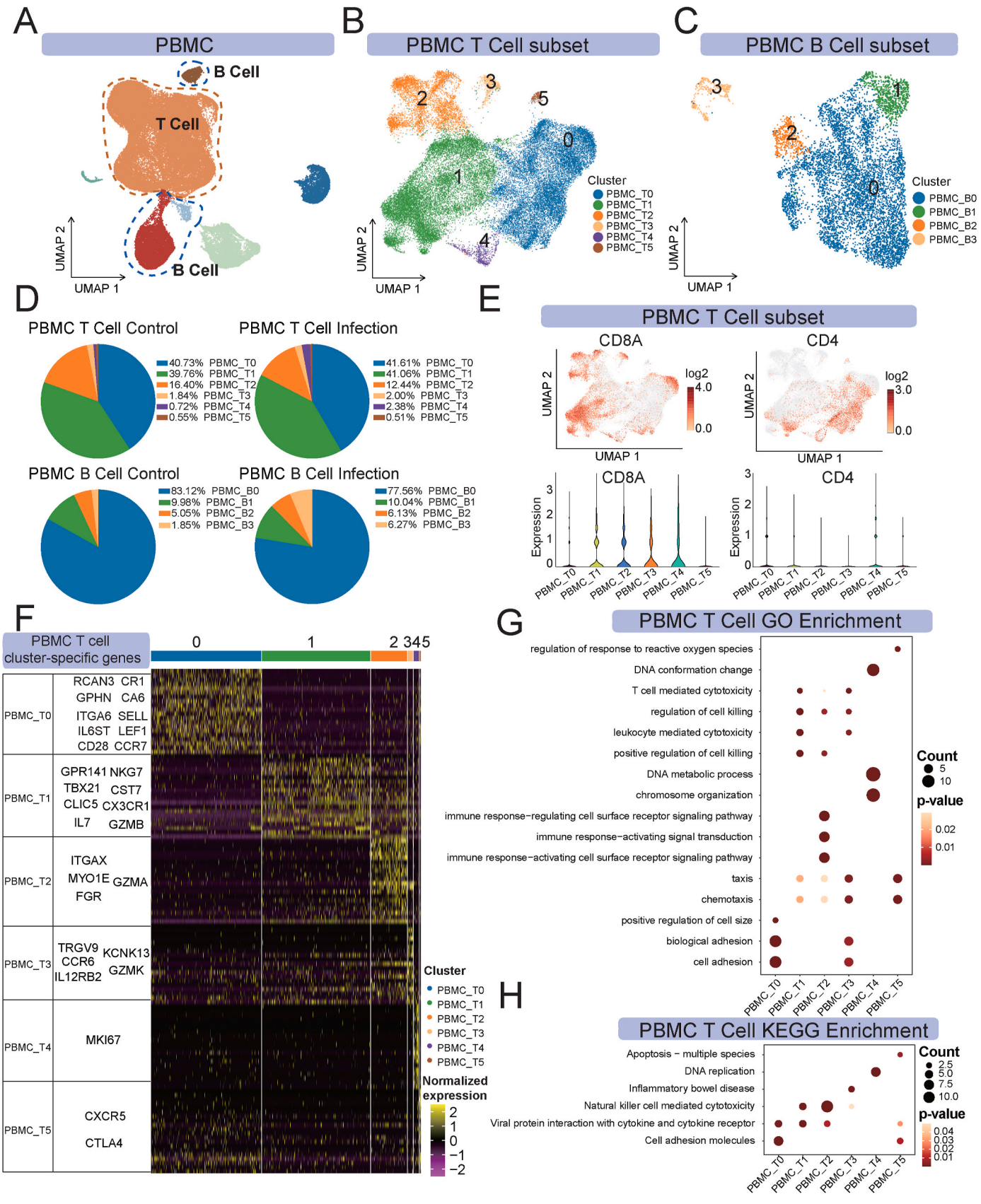

(caption on next page)

Fig. 6. Comprehensive analysis of T and B cell subpopulations in PBMCs
A. Schematic depicting the PBMCs T cells and B cells subcluster analysis.
B. UMAP visualization of T cell subclusters in PBMCs. Each dot represents a cell, colored by subclusters.
C. UMAP visualization of B cell subclusters in PBMCs. Each dot represents a cell, colored by subclusters.
D. Pie charts of T cell (top panel) and B (bottom panel) cell subclusters proportions (%) colored from B or C.
E. The heatmap (top panel) and violin plots (bottom panel) of the expression of CD8A and CD4 in T cell subclusters.
F. The heatmap displays the cluster-specific gene in each subcluster of T cells. Each column represents a cell, and expression values are scaled by normalized expression.
G. Bubble plots of GO biological processes enrichment comparative analysis of T cell subclusters. Bubble size indicates gene ratio; color scale represents p-value.
H. Bubble plots of KEGG enrichment comparative analysis of T cell subclusters. Bubble size indicates gene ratio; color scale represents p-value.

ITM2C, and *TNFRSF17 (BCMA)*. Functional enrichment analysis revealed distinct pathway associations. PBMC_T0 and PBMC_T1 subsets were significantly associated with adhesion processes (biological adhesion, cell adhesion) and cell surface receptor signaling pathways (GO analysis), corresponding to inflammatory pathways such as cytokine-cytokine receptor interaction (KEGG), conversely, PBMC_T4 showed enrichment for DNA metabolic process and chromatin organization (GO) and DNA replication (KEGG) (Fig. 6G and H). PBMC_B2 and PBMC_B3 were exhibited enrichment for protein homeostasis pathways, including cellular response to unfolded protein (GO) and Protein processing in endoplasmic reticulum (KEGG) (Supporting Information 1: Fig. S6D and E).

2.7. Th1 and Th17 differentiation drive the response of PBMCs to CHIKV infection

To delineate developmental trajectories, we performed pseudotime ordering on T and B cells of PBMCs using Monocle 2. Pseudotime trajectory analysis of PBMC T and B cell subsets revealed distinct developmental dynamics. T cells progressed through 17 pseudotime states (Fig. 7A), while B cells traversed 9 states (Fig. 7B), with an accompanying heatmap indicating the direction of pseudotime progression. Subset localization along trajectories showed the T0 subset was enriched in later states (States 9, 11-14), while the T4 subset localized primarily to earlier states (States 1-3, 5, 16-17) (Fig. 7C). Among B cells, the PBMC_B2 subset was enriched in early states (States 1-3), and PBMC_B4 was almost exclusively confined to State 1 (Fig. 7C). CHIKV infection reshaped the distribution of T-cell pseudotime states relative to control samples. The infected group displayed elevated fractions of cells in States 1 and 13, alongside reduced proportions in States 6, 7, 9, and 16 (Supporting Information 1: Fig. S7A). Gene module analysis identified 6 T cell co-expression modules (Fig. 7D). Functional enrichment analysis revealed that cells in pseudotime State 1 corresponded to genes in Module 6, which were enriched in immune response-related pathways such as the immune response and T cell receptor signaling pathway. Genes in the middle pseudotime period mapped to Modules 2, 3, 4, and 5, during which T cells were activating adaptive immunity, as indicated by the engagement of MHC-related pathways. At the pseudotime endpoint, Module 1 genes were significantly associated with T helper 1 (Th1) cell differentiation, the T cell receptor signaling pathway, T helper 17 (Th17) cell differentiation, and the positive regulation of Th17 cell differentiation. Key drivers of this Th1/Th17 signature included NXPE3, LEF1, and NFKBIZ (Supporting Information 1: Fig. S7B).

Gene module analysis identified 6 co-expression modules in B cells. Functional enrichment revealed that early pseudotime B-cell subsets (e.g., PBMC_B0) mapped to modules 1 and 4, which were associated with fundamental immune processes, including immune response, adaptive immune response and immunoglobulin production. In contrast, modules 2, 3, 5, and 6, corresponding to the middle and late pseudotime stages, showed enrichment for post-infection functions including enhanced cell adhesion and the resolution of both innate and adaptive immune responses (Supporting Information 1: Fig. S7E). Key contributing genes included *EYA2*, *SOX5*, and *PRKCH* (Supporting Information 1: Fig. S7C).

3. Discussion

CHIKV, an arbovirus transmitted by *Aedes* mosquitoes, causes severe acute joint pain, chronic arthritis, and systemic infection. Advances in immunological platforms, especially single-cell RNA sequencing (scRNA-seq), have enabled high-resolution profiling of host immune cascades following CHIKV exposure.[33] Understanding this response is crucial for developing effective treatments and vaccines. In this study, we analyzed scRNA-seq data from spleen tissue and PBMCs collected on day 7 post-CHIKV infection in rhesus monkeys, with uninfected monkeys serving as controls. The results showed that significant alterations in neutrophil populations and activation with the spleen. While the overall proportions of T and B cells showed no significant difference between infected and control groups, subsequent analysis revealed altered T cell differentiation. Specifically, Th1 and Th17 differentiation drive the response of PBMCs to CHIKV infection. However, it is important to note that our study's design has a limited sample size (n = 3 per group), a single time point (7 dpi), and a subclinical infection model. It means that our findings are primarily descriptive and hypothesis-generating. The conclusions drawn below should be considered within these evidentiary limits.

This study presents the first comprehensive scRNA-seq atlas of spleen and PBMCs response in rhesus macaques during CHIKV acute infection, characterized by undetectable viral loads in peripheral blood yet remained viral burdens in the spleen (Supporting Information 1: Fig. S1A). Clinical reports indicate that viremia typically resolves within 8 days following symptom onset, with reports of persistence for up to 10-12 days.[34,35] The acute phase of the infection may last until day 14 after the appearance of symptoms.[36] A focus on the acute phase is critical to advancing our understanding of the mechanisms by which the immune system responds to viral infection. The scRNA-seq revealed non-significant increases in splenic $CD4^+$ T cells and PBMC T cells/-monocytes. These findings align with established immunological dynamics: innate effectors (notably NK cells and monocytes) dominate acute viral control,[37] while adaptive immunity (particularly T cell responses) becomes essential for sustained viral clearance during persistence.[18,38,39] Subsequently, we observed massive accumulation of neutrophils within the spleen. Functional enrichment analysis of differentially expressed genes revealed significant enrichment in migration. Neutrophil recruitment to the spleen represents a critical component of innate immunity observed in diverse bacterial and viral infections, mediating the initial response to infection.[40,41]

Pseudotime trajectory analysis of splenic neutrophils revealed their activated terminal state. Accumulating neutrophils occupied terminal pseudotime states characterized by upregulated expression of activation markers *S100A8/S100A*9 and *MMP9*. Robust neutrophil activation is a known driver of NETs formation, a critical antiviral mechanism for controlling viral replication and dissemination. NETs can be induced in murine models of CHIKV infection with distinct responses compared to DENV or ZIKV infection.[15] Consistent with this mechanism, our immunofluorescence analysis of spleen tissue confirmed that NETs ensnare CHIKV particles (Fig. 3G), indicating their role in viral clearance. These results are consistent with the joint tropism of CHIKV, in which persistent infection drives cartilage destruction through the induction of chondrocyte apoptosis and MMP-3/9-mediated extracellular matrix

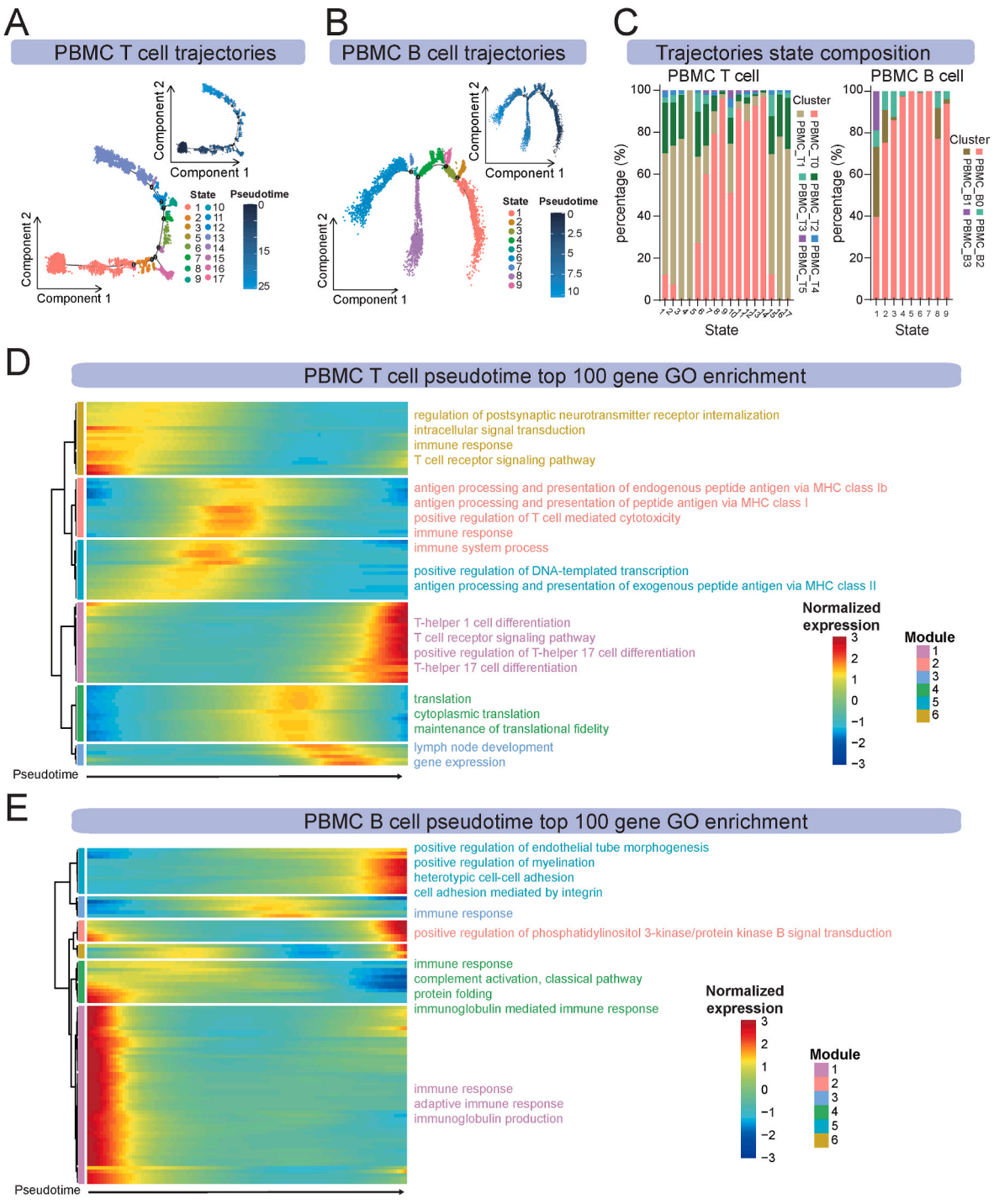

Fig. 7. Trajectory inference and functional characterization of T and B cell progression in PBMC

A. Pseudotime state visualization of T cell subclusters in PBMC, colored by each state. Each dot represents a single cell. The heat map of pseudotime progression is shown in the upper right corner.

B. Pseudotime state visualization of B cell subclusters in PBMC, colored by each state. Each dot represents a single cell. The heat map of pseudotime progression is shown in the upper right corner.

C. Stacked bar chart showing proportional distribution of 6 T cell subclusters (PBMC_T0- PBMC_T5) across 17 pseudotime states (State 1-17) (left panel) and 4 B cell subclusters (PBMC_B0- PBMC_B3) across 9 pseudotime states (State 1-9) (right panel). Color-coding corresponds to subcluster identity as shown in legend.

D. Heatmap of the significantly differentially expressed top 100 genes during progression of T cell in PBMC. The significant GO ($p \leq 0.05$) enriched functions of these genes are shown on the right.

E. Heatmap of the significantly differentially expressed top 100 genes during progression of B cell in PBMC. The significant GO ($p \leq 0.05$) enriched functions of these genes are shown on the right.

degradation.[42] An intriguing finding was the absence of CHIKV RNA in our scRNA-seq data, despite measurable viral loads in bulk splenic tissue. This discrepancy could be explained by several factors. The neutrophils forming NETs might be lost during the scRNA-seq workflow, potentially explaining the absence of CHIKV RNA in our data. However, a more plausible explanation, relates to the sensitivity limits of scRNA-seq and the timing of infection. First, the sensitivity of scRNA-seq for detecting very low-abundance transcripts may be limited compared to bulk qRT-PCR. The viral RNA detected in bulk tissue could originate from a small number of infected cells, potentially falling below the sampling or detection threshold of our single-cell assay. Second, it is possible that by day 7, the peak of active viral transcription has passed, and the remaining viral RNA detected in bulk tissue represents residual, non-replicating viral particles or RNA fragments within phagocytic cells.

While splenic neutrophils effectively mediated viral clearance, the proportions and overall distribution of T and B lymphocytes remained largely unchanged. Subsequent subclustering and pseudotime trajectory analyses revealed no significant infection-induced alterations in splenic lymphocyte subset abundances or pseudotime progression state distributions. DEGs in splenic T and B cells were predominantly enriched for innate immune functions (Figs. 4 and 5). Notably, persistent high splenic viral loads despite undetectable viremia indicate incomplete resolution of acute infection. Excessive neutrophil activation may suppress T/B cell effector functions, and neutrophil hyperactivation could cause collateral tissue damage, further compromising lymphoid responses ([31,43]). In mice during acute infection, splenic neutrophil populations significantly expand. These cells induce immunosuppression by secreting specific cytokines or through direct interactions with other immune cells, thereby inhibiting T cell and other immune effector functions ([43]). Studies in trypanosomiasis models have demonstrated a direct link between neutrophil-derived MMPs and splenic damage.[31]

While PBMC T cell subset proportions showed no significant infection-induced changes, pseudotime trajectory analysis revealed profound state redistribution. Infection group exhibited significantly elevated proportions of cells within State 1 and State 13 compared to controls (Fig. S7A). Critically, State 13 was functionally enriched for Th1 and Th17 differentiation pathways (Fig. 7D). This aligns with established knowledge, CHIKV infection elicits a heterogeneous T-helper lymphocyte response characterized by mixed Th1, Th2, Th17, and Treg profiles.[23,44,45] In murine models, virus-specific $CD4^+$ T cells polarize toward a Th1 phenotype in lymphoid tissue and drive joint inflammation through the release of pro-inflammatory cytokines, whereas Th17-derived IL-17 exacerbates tissue damage by amplifying neutrophil infiltration.[23]

The scRNA-seq has revolutionized the strategic investigation of pathogen-host interactions. Leveraging this approach in a non-human primate (NHP) CHIKV infection model, we constructed the first scRNA-seq atlas of splenic and PBMC responses during transitional phase of infection. We observed that Neutrophils eliminated CHIKV by NETs formation, directly ensnaring viral particles and the differentiation of Th1/Th17 cells in the circulation may further promote viral clearance and generate inflammation. This proposed paradigm of neutrophil-lymphocyte crosstalk requires further functional validation. If confirmed, it could point to novel avenues for therapeutic exploration. However, direct claims remain premature given the descriptive nature of this dataset.

4. Limitations of the study

Our findings should be interpreted considering several limitations. First, the cohort size (n = 3 per group) is small, which may introduce unavoidable bias while adhering to ethical standards for non-human primate research limits statistical power. Second, the analysis is restricted to a single time point (7 dpi), providing only a snapshot and preventing any conclusions about the evolution of immunity over time. Third, the infected animals did not show typical clinical symptoms, suggesting a subclinical model. Thus, our findings may not fully recapitulate the immunopathogenesis of symptomatic human CHIKV disease.Fourth, the lack of detectable viral RNA in our scRNA-seq dataset underscores a key technical limitation of this study. This observation may be attributed to the sensitivity limits of the sequencing assay or the possibility that very few cells remain actively transcribing viral RNA at 7 days post-infection. Consequently, our conclusions are primarily descriptive and should be considered as hypothesis-generating, requiring validation in larger cohorts, longitudinal studies, and human clinical specimens.

5. Materials and methods

5.1. Statements of animal ethics and biosafety

All animal procedures were approved by the Institutional Animal Care and Use Committee of the Institute of Medical Biology, Chinese Academy of Medical Sciences & Peking Union Medical College (IMBCAMS&PUMC) (approval number: DWSP20210006). Animal infection studies and handling of infectious samples were conducted in the ABSL-3 facility at the National Kunming high-level Biosafety Primate Research Center, Yunnan, China.

5.2. CHIKV strains and animal experimental procedures

The viral strain (Accession: MH670649.1) was maintained by the Institute of Medical Biology, Chinese Academy of Medical Sciences & Peking Union Medical College (IMBCAMS&PUMC). CHIKV was propagated in Vero cells through continuous passage, and its titer was determined using plaque-forming unit (PFU) assay to ensure accurate quantification.

Six adult rhesus monkeys were randomly divided into infection group and control group. All animals were screened for CHIKV antibodies/viremia before testing. Throughout the experiment, the animals were kept in isolation and with standardized diet and water. The infected group received an intramuscular challenge of 2×10^7 PFU CHIKV in the hind limbs, while the controls received an equivalent volume of Phosphate Buffer Saline (PBS, Servicebio, Cat# G4202-500 ML). During the experiment, we collected blood samples from rhesus monkeys and measured their body temperature and body weight. We also conducted clinical observations on indicators including behavior and mentation, food and water intake, and fecal characteristics. Any abnormalities were documented accordingly; otherwise, findings were recorded as "Normal."

5.3. Sample collection and preparation of single cell suspensions

On the 7th day after injection, the experimental animals were euthanized, whole blood and fresh spleen tissues were collected, single-cell suspensions were prepared and scRNA-seq was performed. (Fig. 1A). PBMCs were prepared from whole blood (5 mL) using the Ficoll-Paque™ Plus kit (Cytiva, Cat#17144003). Whole blood was diluted 1:1 with sterile PBS buffer in a 50 mL centrifuge tube. The diluted blood sample carefully layered over an equal volume of Ficoll-Paque™ PLUS without disturbing the interface. Samples were centrifuged at $400 \times g$ for 20 min at room temperature (acceleration/deceleration: low). The PBMC layer was collected and washed with PBS by centrifugation at $300 \times g$ for 10 min. The pellet was washed twice with phosphate-buffered saline (PBS) containing 1% fetal bovine serum (FBS; Gibco, Cat# A5669701), then resuspended in PBS/1% FBS for downstream processing.

Fresh spleen tissue was dissected into small fragments with sterile scissors and transferred to Krebs Ringer solution with glucose (Merck, Cat# K4002-10X1L) pre-warmed to 37 °C, containing 0.05% (w/v) collagenase (Merck, Cat# C4-28-100 MG). The tissue was manually mechanically dissociated until no large fragments remained. The resulting homogenate was filtered through a 40-μm cell strainer twice.

The filtrate was centrifuged at 300×*g* for 10 min at room temperature. The pellet was washed twice with phosphate-buffered saline (PBS) containing 1% fetal bovine serum (FBS; Gibco, Cat# A5669701), then resuspended in PBS/1% FBS for downstream processing.

5.4. Single-cell library preparation & sequencing

Single-cell suspensions were processed using the Chromium Next GEM Single Cell 3′ Reagent Kits v3.1 (10x Genomics, Cat# PN-1000123, PN-1000190), targeting a cell capture estimate of 10,000 cells per sample. Cells were co-encapsulated with barcoded Gel Beads and master mix in the Chromium Controller to form Gel Beads-in-Emulsion (GEMs). Within GEMs, reverse transcription synthesized barcoded cDNA following: 1) Gel Bead dissolution, 2) cell lysis, and 3) mRNA capture. Library construction followed manufacturer protocols (10x Genomics, www.10xgenomics.com). Libraries were sequenced on an Illumina NovaSeq 6000 (150 bp paired-end) yielding ~120 Gb/sample.

5.5. Bioinformatics Analysis

Raw sequencing data underwent quality assessment using FastQC (v0.11.2, www.bioinformatics.babraham.ac.uk/projects/fastqc/). Cell Ranger software suite (www.10xgenomics.com/support/software/cell-ranger) was used for reference-based alignment to the rhesus macaque genome (*Macaca mulatta*, assembly Mmul_10, Ensembl) and initial processing, including barcode filtering, UMI counting, and gene expression matrix generation. For quality control, we filtered out cells with fewer than 200 genes, fewer than 2000 counts, or more than 11,000 counts, and more than 10% mitochondrial UMIs. Downstream analyses were performed using Seurat (v5, satijalab.org/seurat/) and included, including dimensionality reduction (PCA, UMAP/t-SNE), unsupervised clustering, cell type annotation and differential expression genes (DEGs) analysis. Functional enrichment analyses on differentially expressed genes (DEGs) included: Gene Ontology (GO) and KEGG pathway analysis (clusterProfiler v4.4.4, github.com/YuLab-SMU/clusterProfiler), Gene Set Enrichment Analysis (GSEA v4.2.3, www.gsea-msigdb.org/gsea/downloads.jsp). Single-cell trajectories were constructed using Monocle2 (v2.4.0).[46] Data visualization was performed using ggplot2 (v3.4.4, ggplot2.tidyverse.org) and GraphPad Prism (v8, www.graphpad.com).

5.6. Measurement of viral load

For viral inactivation, 200 μL whole blood was immediately mixed with 600 μL TRI Reagent™ (Invitrogen, Cat# AM9738) (1:3 ratio). Similarly, ~50 mg spleen tissue was homogenized in 800 μL TRI Reagent™. Total RNA was extracted from both matrices using the Upure Virus RNA Plus Kit (Biokeystone, M2006P-96 KF). The qRT-PCR was performed using TaqMan™ Fast Virus 1-Step Master Mix (Thermo Fisher Scientific, Cat# 4444434) on a CFX384 Touch system (Bio-Rad). CHIKV E-gene primers and probe: Forward: 5'-CTCATACCGCATCCGCATCAG-3; Reverse: 5'-ACA TTGGCCCCACAATGAATTTG-3'; Probe: 5'-FAM-TCCTTAACTGTGACGGCATGGTCGCC-BHQ1-3'. Absolute quantification was achieved using a standard curve generated from serially diluted plasmid (10^9-10^1 copies/μL) containing the target amplicon.

5.7. Histopathologic and immunohistochemistry (IHC)analysis

Formalin-fixed paraffin-embedded (FFPE) sections (5 μm) were prepared for hematoxylin and eosin (H&E) staining. The stained sections were scanned using 3D HISTECH(Hungary). The slides were evaluated by an experienced pathologist in a double-blind manner. Scoring based on 4 indicators: 1. Diffuse lymphocyte infiltrates. 2. Diffuse hemorrhage. 3. Activation in germinal center 4. Reduction in germinal centers. Each indicator was scored as 0, deficient; 1, mild; 2, moderate; 3, moderate diet; and 4, severe.

5.8. Immunofluorescence (IF) staining for NETs

FFPE spleen sections underwent multiplex immunofluorescence staining for NETs visualization using a tyramide signal amplification (TSA) approach. Primary antibodies included: Anti-Myeloperoxidase (MPO) (ABclonal, Cat# A1374), Anti- H3Cit (GeneTex, Cat# GTX122148-S) and Anti-Chikungunya Virus (Novus Biologicals, Cat# 6A11). Nuclear counterstaining used 4′,6-diamidino-2-phenylindole (DAPI; Abcam, Cat# ab104139). The staining protocol proceeded sequentially as follows: 1) Primary antibody incubation. 2) horseradish peroxidase (HRP)-conjugated secondary antibody incubation. 3) Tyramide-fluorophore conjugation (PerkinElmer OPAL™ reagents. 4) Microwave-assisted antibody stripping (10 mM sodium citrate pH 6.0, 95 °C). 5) Repetition of cycle for subsequent targets. Stained sections were imaged using a Leica Stellaris confocal with consistent acquisition settings. Two independent, blinded histopathologists performed whole-slide scanning and selected representative fields for analysis.

5.9. Complete blood count (CBC) analysis

The venous blood samples (1 mL) were collected from each NHP using vacuum tubes containing K_2EDTA. CBC analysis was performed using an automated hematology analyzer (BC-5000, Mindray).

5.10. Statistical analysis

All statistical analyses were conducted in R (v 4.3.0, www.r-project.org). Statistical significance was defined as $p \leq 0.05$. Specifically, comparisons of cell proportions, viral load, H&E scores, IHC positive cell counts, and CBC between the infected and control groups were performed using the Mann-Whitney test. The p-values for all other analyses were generated by the software tools specified in the Bioinformatics Analysis section. Each figure legend provides details about the specific statistical analysis. Figures were generated using Adobe Illustrator, as well as the R packages ggplot2 and GraphPad Prism 8.

CRediT authorship contribution statement

Yun Yang: Writing – original draft, Validation, Software, Methodology, Formal analysis, Data curation. **Qing Huang:** Writing – original draft, Validation, Supervision, Software, Methodology, Formal analysis. **Hao Yang:** Writing – original draft, Validation, Software, Methodology, Formal analysis, Data curation. **Yanan Zhou:** Visualization, Investigation, Formal analysis, Data curation. **Junbin Wang:** Validation, Methodology, Investigation. **Cong Tang:** Validation, Methodology, Data curation. **Wenhai Yu:** Software, Methodology, Investigation. **Haixuan Wang:** Methodology, Investigation. **Daoju Wu:** Supervision, Methodology. **Hongyu Chen:** Software, Formal analysis. **Bai Li:** Methodology, Data curation. **Wenqi Quan:** Supervision. **Jiandong Shi:** Writing – review & editing, Visualization, Supervision, Project administration, Investigation, Conceptualization. **Qiangming Sun:** Writing – review & editing, Project administration, Funding acquisition, Conceptualization. **Shuaiyao Lu:** Writing – review & editing, Resources, Project administration, Funding acquisition, Conceptualization.

Funding

This work was supported partially by grants from the National Science and Technology Major Project (2025ZD01900706); Major project of basic research in Yunnan Province (202401BC070008); Science and Technology Leading Talent Program of Yunnan Province (202405AB350002); High-Level Medical Talent Training Program of Yunnan Province (L-2024018).

Declaration of competing interest

The authors declare that they have no known competing financial interests or personal relationships that could have appeared to influence the work reported in this paper.

Acknowledgements

We appreciate services of all the staff at the National Kunming High-level Biosafety Primate Research Center.

Appendix A. Supplementary data

Supplementary data to this article can be found online at https://doi.org/10.1016/j.jve.2026.100624.

Abbreviations

CHIKV	Chikungunya virus
NHP	Non-human primate
ABLS-3	Animal biosafety level 3
PBS	Phosphate-buffered saline
H&E	Hematoxylin-eosin staining
DEGs	Differentially expressed genes
GO	Gene Ontology
KEGG	Kyoto Encyclopedia of Genes and Genomes
Th1	T helper 1
Th17	T helper 17
RT-qPCR	Reverse Transcription quantitative Polymerase Chain Reaction

Data availability

Data will be made available on request.

References

1. Kril V, Aïqui-Reboul-Paviet O, Briant L, Amara A. New insights into Chikungunya virus infection and pathogenesis. *Annual review of virology*. 2021;8(1):327–347.
2. Paul BJ, Sadanand S. Chikungunya infection: a Re-emerging epidemic. *Rheumatol Ther*. 2018;5(2):317–326.
3. Zaid A, Gérardin P, Taylor A, Mostafavi H, Malvy D, Mahalingam S. Chikungunya arthritis: implications of acute and chronic inflammation mechanisms on disease management. *Arthritis Rheumatol*. 2018;70(4):484–495.
4. Burt F, Chen W, Mahalingam S. Chikungunya virus and arthritic disease. *Lancet Infect Dis*. 2014;14(9):789–790.
5. Chopra A, Venugopalan A. Chikungunya and other viral arthritis. *Best Pract Res Clin Rheumatol*. 2025;39(2), 102068.
6. Fred A, Fianu A, Béral M, et al. Individual and contextual risk factors for chikungunya virus infection: the SEROCHIK cross-sectional population-based study. *Epidemiol Infect*. 2018;146(8):1056–1064.
7. Brito C, Falcão MB, de Albuquerque M, Cerqueira-Silva T, Teixeira MG, Franca RFO. Chikungunya: from Hypothesis to evidence of increased severe disease and fatalities. *Viruses*. 2025;17(1).
8. de Lima Cavalcanti TYV, Pereira MR, de Paula SO, Franca RFO. A review on Chikungunya Virus epidemiology, pathogenesis and Current vaccine development. *Viruses*. 2022;14(5).
9. Couderc T, Chrétien F, Schilte C, et al. A mouse model for Chikungunya: young age and inefficient type-I interferon signaling are risk factors for severe disease. *PLoS Pathog*. 2008;4(2):e29.
10. Schilte C, Couderc T, Chretien F, et al. Type I IFN controls chikungunya virus via its action on nonhematopoietic cells. *J Exp Med*. 2010;207(2):429–442.
11. Chaaitanya IK, Muruganandam N, Sundaram SG, et al. Role of proinflammatory cytokines and chemokines in chronic arthropathy in CHIKV infection. *Viral Immunol*. 2011;24(4):265–271.
12. Hoarau JJ, Jaffar Bandjee MC, Krejbich Trotot P, et al. Persistent chronic inflammation and infection by Chikungunya arthritogenic alphavirus in spite of a robust host immune response. *J Immunol*. 2010;184(10):5914–5927.
13. Young AR, Locke MC, Cook LE, et al. Dermal and muscle fibroblasts and skeletal myofibers survive chikungunya virus infection and harbor persistent RNA. *PLoS Pathog*. 2019;15(8), e1007993.
14. Thiam HR, Wong SL, Wagner DD, Waterman CM. Cellular mechanisms of NETosis. *Annu Rev Cell Dev Biol*. 2020;36:191–218.
15. Hiroki CH, Toller-Kawahisa JE, Fumagalli MJ, et al. Neutrophil extracellular traps effectively control Acute Chikungunya Virus infection. *Front Immunol*. 2019;10:3108.
16. Smith PK, Wang SZ, Dowling KD, Forsyth KD. Leucocyte populations in respiratory syncytial virus-induced bronchiolitis. *J Paediatr Child Health*. 2001;37(2):146–151.
17. Agraz-Cibrian JM, Giraldo DM, Mary FM, Urcuqui-Inchima S. Understanding the molecular mechanisms of NETs and their role in antiviral innate immunity. *Virus Res*. 2017;228:124–133.
18. Torres-Ruesta A, Teo TH, Chan YH, Rénia L, Ng LFP. Pathogenic Th1 responses in CHIKV-induced inflammation and their modulation upon Plasmodium parasites co-infection. *Immunol Rev*. 2020;294(1):80–91.
19. Nakaya HI, Gardner J, Poo YS, Major L, Pulendran B, Suhrbier A. Gene profiling of Chikungunya virus arthritis in a mouse model reveals significant overlap with rheumatoid arthritis. *Arthritis Rheum*. 2012;64(11):3553–3563.
20. Yamada H, Nakashima Y, Okazaki K, et al. Preferential accumulation of activated Th1 cells not only in rheumatoid arthritis but also in osteoarthritis joints. *J Rheumatol*. 2011;38(8):1569–1575.
21. Bazzazi H, Aghaei M, Memarian A, Asgarian-Omran H, Behnampour N, Yazdani Y. Th1-Th17 Ratio as a new Insight in rheumatoid Arthritis disease. *Iran J Allergy Asthma Immunol*. 2018;17(1):68–77.
22. Tang YY, Wang DC, Chen YY, Xu WD, Huang AF. Th1-related transcription factors and cytokines in systemic lupus erythematosus. *Front Immunol*. 2023;14, 1305590.
23. Liu X, Poo YS, Alves JC, et al. Interleukin-17 contributes to Chikungunya virus-induced disease. *mBio*. 2022;13(2), e0028922.
24. Wang C, Huyan T, Zhou X, et al. Development of single-cell transcriptomics and its application in COVID-19. *Viruses*. 2022;14(10).
25. Ratnasiri K, Wilk AJ, Lee MJ, Khatri P, Blish CA. Single-cell RNA-seq methods to interrogate virus-host interactions. *Semin Immunopathol*. 2023;45(1):71–89.
26. Lin D, Tang C, Wang J, et al. Multiorgan proteomic analysis of infected animal models predict potential host factors for chikungunya virus. *MedComm*. 2025;6(1), e70013.
27. Chen H, Shi J, Tang C, et al. CHIKV infection drives shifts in the gastrointestinal microbiome and metabolites in rhesus monkeys. *Microbiome*. 2024;12(1):161.
28. Qu J, Yang F, Zhu T, et al. A reference single-cell regulomic and transcriptomic map of cynomolgus monkeys. *Nat Commun*. 2022;13(1):4069.
29. Han L, Wei X, Liu C, et al. Cell transcriptomic atlas of the non-human primate Macaca fascicularis. *Nature*. 2022;604(7907):723–731.
30. Hu C, Li T, Xu Y, et al. CellMarker 2.0: an updated database of manually curated cell markers in human/mouse and web tools based on scRNA-seq data. *Nucleic Acids Res*. 2023;51(D1). D870-d6.
31. Pham HTT, Magez S, Choi B, Baatar B, Jung J, Radwanska M. Neutrophil metalloproteinase driven spleen damage hampers infection control of trypanosomiasis. *Nat Commun*. 2023;14(1):5418.
32. Evrard M, Kwok IWH, Chong SZ, et al. Developmental analysis of bone marrow neutrophils reveals populations specialized in expansion, trafficking, and effector functions. *Immunity*. 2018;48(2), 364-79.e8.
33. Brito RMdM, de Melo MF, Fernandes JV, et al. Acute Chikungunya virus infection triggers a diverse range of T helper lymphocyte profiles. *Viruses*. 2024;16(9).
34. Win MK, Chow A, Dimatatac F, Go CJ, Leo YS. Chikungunya fever in Singapore: acute clinical and laboratory features, and factors associated with persistent arthralgia. *J Clin Virol : the official publication of the Pan American Society for Clinical Virology*. 2010;49(2):111–114.
35. Appassakij H, Khuntikij P, Kemapunmanus M, Wutthanarungsan R, Silpapojakul K. Viremic profiles in asymptomatic and symptomatic chikungunya fever: a blood transfusion threat? *Transfusion*. 2013;53(10 Pt 2):2567–2574.
36. Bartholomeeusen K, Daniel M, LaBeaud DA, et al. Chikungunya fever. *Nat Rev Dis Primers*. 2023;9(1):17.
37. Tanabe ISB, Tanabe ELL, Santos EC, et al. Cellular and molecular immune response to Chikungunya virus infection. *Front Cell Infect Microbiol*. 2018;8:345.
38. Burt FJ, Chen W, Miner JJ, et al. Chikungunya virus: an update on the biology and pathogenesis of this emerging pathogen. *Lancet Infect Dis*. 2017;17(4):e107–e117.
39. Agarwal R, Chang J, Côrtes FH, et al. Chikungunya virus-specific CD4(+) T cells are associated with chronic chikungunya viral arthritic disease in humans. *Cell Rep Med*. 2025;6(5), 102134.
40. Papayannopoulos V. Neutrophil extracellular traps in immunity and disease. *Nat Rev Immunol*. 2018;18(2):134–147.
41. Zuo Y, Zuo M, Yalavarthi S, et al. Neutrophil extracellular traps and thrombosis in COVID-19. *J Thromb Thrombolysis*. 2021 Feb;51(2):446–453.
42. Legros V, Belarbi E, Jeannin P, et al. Use of recombinant Chikungunya Virus expressing nanoluciferase to identify chondrocytes as target cells in an immunocompetent mouse model. *J Infect Dis*. 2025 Aug 14;232(2):e223–e233.
43. Liao C, Luo S, Liu X, et al. Siglec-F(+) neutrophils in the spleen induce immunosuppression following acute infection. *Theranostics*. 2024;14(6):2589–2604.
44. Teo TH, Lum FM, Claser C, et al. A pathogenic role for CD4+ T cells during Chikungunya virus infection in mice. *J Immunol*. 2013;190(1):259–269.
45. Ferreira AS, Baldoni NR, Cardoso CS, Oliveira CDL. Biomarkers of severity and chronification in chikungunya fever: a systematic review and meta-analysis. *Rev Inst Med Trop Sao Paulo*. 2021;63, e16.
46. Qiu X, Mao Q, Tang Y, et al. Reversed graph embedding resolves complex single-cell trajectories. *Nat Methods*. 2017;14(10):979–982.